

Implementation of A Coupled Thermo-piezoelectric-mechanical Model in The LQG Controller Design for Smart Composite Shells

HEUNG SOO KIM,^{1,*} ADITI CHATTOPADHYAY¹ AND CHANGHO NAM²

¹*Department of Mechanical and Aerospace Engineering, Arizona State University, Tempe, AZ 85287-6106, USA*

²*Department of Manufacturing and Aeronautical Engineering Technology, ASU East, Mesa, AZ 85212, USA*

ABSTRACT: The present paper aims to develop a completely coupled thermo-piezoelectric-mechanical theory, based on an improved layerwise displacement field and higher order electrical and temperature fields, to study dynamic response and control of smart composite shells. A variational principle, addressing the interaction between thermal, piezoelectric and mechanical fields, is used to derive the governing equations of equilibrium. Finite element technique is used to ensure application to practical geometry and boundary conditions. Numerical analysis is conducted for simply supported cylindrical shells with distributed self-sensing piezoelectric actuators. Control authority is investigated using Linear Quadratic Gaussian (LQG) theory. Parametric studies are conducted to investigate the effect of two-way coupling, placement of actuators, coupling and flexibility of the primary structure.

Key Words: smart composite shell, two-way coupling, LQG controller, layerwise displacement

INTRODUCTION

THE development of smart composites offers great potential in advanced aerospace structural applications. Piezoelectric materials are employed as both actuators and sensors in the development of these structures by taking advantage of direct and converse piezoelectric effects. Passive and active control using piezoelectric materials has traditionally been studied using classical laminate theory (CLT) which ignores the transverse shear effects in structural modeling (Crawley and Luis, 1987; Lee, 1990). First order shear deformation theory has been used to develop a dynamic model of piezothermoelastic shell laminate (Tzou and Bao, 1995). A refined hybrid laminate theory that combines the layerwise theory and an equivalent single-layer theory (ESL) along with linear piezoelectricity was developed to model smart composite laminates (Mitchell and Reddy, 1995a,b). A higher order theory, which proved to be computationally more efficient and capable of accurately capturing the transverse shear effects, for both thin and moderately thick laminates, was developed by Zhou et al. (2000). In the analysis of smart structures, the coupling issues associated with thermal, piezoelectric and mechanical fields play an important role. However, these issues are not adequately addressed in most applications. In most of the work, one-way coupling that only considers the effect of a known field on

another field is used. The two-way coupling between piezoelectric and mechanical fields was incorporated in the hybrid plate and shell theory developed by Mitchell and Reddy (1995a,b). Anderson and Hagood (1994) investigated passive damping and self-sensing actuators using coupled electromechanical modeling. A two-way coupling effect on the dynamic response are studied by Thornburgh and Chattopadhyay (2001).

Thermal effect was studied by Mindlin (1974) and Mukherjee and Sinha (1993). Following their work, the piezothermoelastic behavior of composite plates was addressed by Tauchert (1992) using CLT and by Lee and Saravanos (1996, 1997) using layerwise theory. In these works, a prescribed thermal field was used to study the effect on mechanical and piezoelectric fields. The mutual interactions between thermal and mechanical fields as well as thermal and piezoelectric fields were ignored. Recently, a coupled thermal-piezoelectric-mechanical (t-p-m) model was developed by Chattopadhyay et al. (1998a,b) to address the two-way coupling issues associated with smart composites under thermal loads. A linear temperature field was used and only quasi-static response was presented (Chattopadhyay et al., 1998a). This was followed by the development of a higher order temperature field to accurately model the temperature distribution through laminates of moderately thick constructions (Chattopadhyay et al., 1998b). Recently, an improved layer-wise theory was developed to accurately predict interlaminar stresses in shell structures (Zhou and Chattopadhyay, 2001). This theory was extended to model static response of shell structures with patched

*Author to whom correspondence should be addressed.

piezo actuators by including thermo-piezoelectric-mechanical coupling (Kim et al., 2001). The objective of the present paper is to further extend the coupled theory to model the dynamic response of smart composite shells. The improved layerwise theory is used to describe the displacement field to properly account for the transverse shear stresses that are important in composites. The governing equations are derived by applying the principle of free energy and variational principles. The finite element technique is employed to implement the mathematical model. Numerical results are presented on the dynamic response of composite cylindrical shells with surface bonded piezoelectric actuators. Control authority is investigated using Linear Quadratic Gaussian (LQG) controller. Parametric studies are conducted to investigate the effects of two-way coupling, actuator location, and bending-torsion coupling of the laminated composite shell.

STRUCTURAL MODELING

For the elastic system with piezoelectric materials as shown in Figure 1, the total free energy of the structure can be written as

$$F(\varepsilon_{ij}, E_i, \theta) = \frac{1}{2} c_{ijkl} \varepsilon_{ij} \varepsilon_{kl} - e_{ijk} E_i \varepsilon_{jk} - \frac{1}{2} b_{ij} E_i E_j - k_{ij} \theta \varepsilon_{ij} - d_i E_i \theta - \frac{1}{2} a_T \theta^2 \quad (1)$$

where ε_{ij} are the components of the strain tensor, E_i are the components of the electric field vector and θ is the temperature rise from the initial temperature T_0 . The quantities c_{jkl} and e_{ijk} represent elastic and piezoelectric

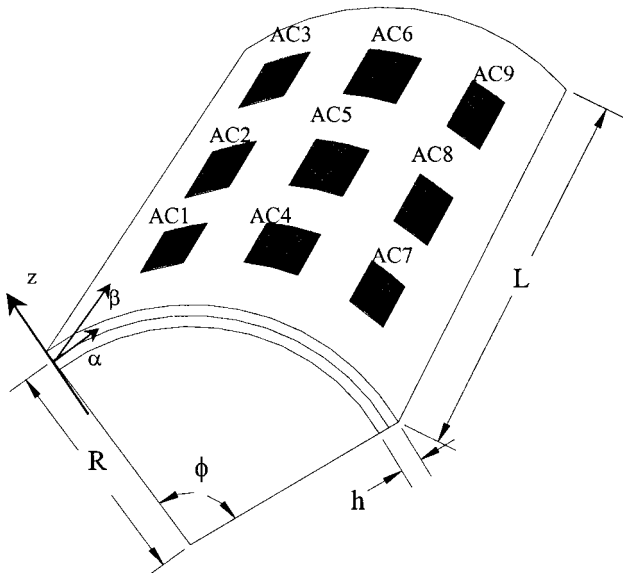


Figure 1. Geometry of cylindrical shell with patched PZTs.

constants, respectively and b_{ij} is dielectric permittivity. The quantities k_{ij} and d_i refer to thermal-mechanical and thermal-piezoelectric coupling constants, respectively, and a_T is defined as c_E/T_0 , where c_E is heat capacity. Piezoelectric material with linear constitutive relations is considered in the present work. This implies constant material coefficients. The constitutive relations can be written as follows.

$$\begin{aligned} \sigma_{ij} &= \frac{\partial F}{\partial \varepsilon_{ij}} = c_{ijkl} \varepsilon_{kl} - e_{ijk} E_k - k_{ij} \theta \\ D_i &= -\frac{\partial F}{\partial E_i} = e_{ijk} \varepsilon_{jk} + b_{ij} E_j + d_i \theta \\ S &= -\frac{\partial F}{\partial \theta} = k_{ij} \varepsilon_{ij} + d_i E_i + a_T \theta \end{aligned} \quad (2)$$

where σ_{ij} , and D_i are the components of the stress tensor and the electric displacement vector, respectively, and S is entropy density. Based on linear piezoelectricity, E_i is derivable from a scalar potential function ϕ as follows.

$$E_i = -\phi_{,i} \quad (i = 1, 2, 3) \quad (3)$$

The governing equations are now derived using variational principles as follows,

$$\begin{aligned} \delta \pi_u &= - \int_0^{t_0} \int_V (\rho \ddot{u}_i \delta u_i + \gamma \dot{r}_i \delta u_i + \sigma_{ij} \delta \varepsilon_{ij}) dV dt \\ &\quad + \int_0^{t_0} \int_S t_i \delta u_i dS dt = 0 \\ \delta \pi_\phi &= - \int_0^{t_0} \int_V D_i \delta \phi_{,i} dV dt + \int_0^{t_0} \int_S q_e \delta \phi dS dt = 0 \\ \delta \pi_\theta &= \int_0^{t_0} \int_V (\kappa_{ij} \theta_{,i} \delta \theta_{,j} + \dot{S} T_0 \delta \theta) dV dt \\ &\quad + \int_0^{t_0} \int_S q_t \delta \theta dS dt = 0 \end{aligned} \quad (4)$$

where π_u , π_ϕ and π_θ denote the energy functionals of mechanical, electrical and thermal fields, respectively. The quantities ρ , γ and κ_{ij} , denote mass density, material damping constant and material thermal conductivity, respectively. The quantity \dot{S} denotes the time derivative of S , t_i represents the components of the traction vector and q_e represents charge density. The quantity q_t , represents specific heat flux or convective heat flux defined as follows.

$$q_t = h_v (\theta + T_0 - T_\infty) \quad (5)$$

In Equation (5), h_v is the thermal convection coefficient and T_0 and T_∞ are initial and environment temperature, respectively.

Improved Layerwise Deformation Theory

Consider a shell element with N laminae described in orthogonal coordinates, α and β , along the shell mid-surface as shown in Figure 1. The thickness co-ordinate, z , is measured from the mid-surface and R_α and R_β are the radii of curvature of the α and β -curves. The area of an infinitesimal rectangle dS and the volume of an infinitesimal parallelepiped dv are defined as follows.

$$\begin{aligned} dS &= A_\alpha(1 + z/R_\alpha)A_\beta(1 + z/R_\beta)d\alpha d\beta \\ dv &= A_\alpha(1 + z/R_\alpha)A_\beta(1 + z/R_\beta)dz \end{aligned} \quad (6)$$

where A_α and A_β are the coefficients of the first fundamental form of the shell reference surface. For cylindrical shell, R_β is infinite and A_β is unity. In the present paper, the equilibrium of the shell element is described using layerwise displacement field as follows.

$$\begin{aligned} U_\alpha^k &= \left(1 + \frac{z}{R_\alpha}\right)u_\alpha + A_\alpha^k(z)\phi_\alpha + B_\alpha^k(z)\phi_\beta \\ &\quad + C_\alpha^k(z)W_{,\alpha} + D_\alpha^k(z)w_{,\beta} \\ U_\beta^k &= \left(1 + \frac{z}{R_\beta}\right)u_\beta + A_\beta^k(z)\phi_\alpha + B_\beta^k(z)\phi_\beta \\ &\quad + C_\beta^k(z)W_{,\alpha} + D_\beta^k(z)w_{,\beta} \\ U_z^k &= w \end{aligned} \quad (7)$$

In Equation (7), the layerwise coefficients (A_α^k, B_α^k and so on) are obtained by enforcing displacement and stress continuity condition at each interface and traction free boundary conditions at free surfaces. The details of this procedure are described in Kim et al. (2001). It must be noted that the structural unknowns describing the mechanical field, ranging from the first lamina to the N th lamina, are reduced to a total of five variables, which are same as those used in first order shear deformation theory. Thus, the developed approach renders the number of structural variables independent of the number of laminae. All terms on the order of the thickness coordinate-to-radius are retained in the formulation, which makes the current approach applicable to the analysis of thick shell structures.

Higher Order Piezoelectric Field

The electric field in piezoelectric layers is conventionally modeled using a linear potential assumption to describe the field distribution. That is, the electric potential is described as a linear function of the thickness coordinate, which leads to a constant electric field through the thickness direction. However, such a distribution does not satisfy the equipotential boundary conditions. Therefore, a cubic distribution of the potential field along the thickness of piezoelectric

layers is assumed to satisfy the surface boundary condition of applied voltage (Zhou et al., 2000). The potential field (ϕ^j) for the j th layer can be written as follows.

$$\begin{aligned} \phi^j(\alpha, \beta, z) &= \phi_0^j(\alpha, \beta) - (z - z_0^j)E_z^j(\alpha, \beta) + 4\left(\frac{z - z_0^j}{h^j}\right)^2 \\ &\quad \times \left[(z - z_0^j)\left(\frac{\bar{\phi}^j}{h^j} + E_z^j(\alpha, \beta)\right) - \phi_0^j(\alpha, \beta) \right] \end{aligned} \quad (8)$$

where ϕ_0^j is the potential of a point in the mid-plane of the k th piezoelectric layer. The quantity E_z^j denotes the electric field at mid-plane and the term $-(z - z_0^j)E_z^j$ is used to address the linear potential distribution through the thickness. The last term in Equation (8) represents the higher order modification, addressing the nonuniform potential variation through the thickness while satisfying the equipotential surface boundary conditions prescribed at the electrodes. The quantity $\bar{\phi}^j$ denotes the potential difference between the top and the bottom electrodes covering the j th piezoelectric transducer and z_0^j and h^j denote the mid-plane position and the thickness of the j th piezoelectric layer, respectively.

Higher Order Temperature Field

It is important to note that although a linear temperature field can address the in-plane temperature distribution, it cannot satisfy the surface thermal boundary conditions. Thus, temperature variations through the thickness, which produce the most important bending deformation, cannot be modeled accurately using linear temperature field. To address nonuniform temperature distribution through the laminate thickness, the temperature field is described using a cubic function of the thickness coordinate. By imposing surface boundary conditions of heat flux, the higher order temperature field can be written as follows.

$$\begin{aligned} \theta(\alpha, \beta, z) &= -\left(\frac{z^2}{2H} \frac{q_t - q_b}{\kappa_{33}} + \frac{2z^3}{3H^2} \frac{q_t + q_b}{\kappa_{33}}\right) \\ &\quad + \theta_0(\alpha, \beta) + \left(z - \frac{4}{3H^2}z^3\right)\theta_1(\alpha, \beta) \end{aligned} \quad (9)$$

where the quantities q_t and q_b indicate the heat flux applied on top and bottom surfaces, respectively. The quantity κ_{33} denotes thermal conductivity through the thickness and H represents the total thickness of the laminate. The higher order temperature field defines a nonuniform cubic distribution through the thickness

of the structure. Further details are available in Zhou et al. (2000).

Finite Element Model

After finite element implementation, the governing equations of the completely coupled (t-p-m) theory, based on the improved layer-wise displacement field and the higher order electric and temperature field, are obtained and are written in matrix form as follows.

$$\begin{bmatrix} M & 0 & 0 \\ 0 & 0 & 0 \\ 0 & 0 & 0 \end{bmatrix} \begin{Bmatrix} \ddot{u}_u^e \\ \ddot{u}_\phi^e \\ \ddot{u}_\theta^e \end{Bmatrix} + \begin{bmatrix} C_{uu} & 0 & 0 \\ 0 & 0 & 0 \\ C_{\theta u} & C_{\theta\phi} & C_{\theta\theta} \end{bmatrix} \begin{Bmatrix} \dot{u}_u^e \\ \dot{u}_\phi^e \\ \dot{u}_\theta^e \end{Bmatrix} + \begin{bmatrix} K_{uu} & K_{u\phi} & K_{u\theta} \\ K_{\phi u} & K_{\phi\phi} & K_{\phi\theta} \\ 0 & 0 & K_{\theta\theta} \end{bmatrix} \begin{Bmatrix} u_u^e \\ u_\phi^e \\ u_\theta^e \end{Bmatrix} = \begin{Bmatrix} F_u \\ F_\phi \\ F_\theta \end{Bmatrix} \quad (10)$$

where u_u^e and u_θ^e denote the displacement and temperature unknowns of the element, respectively and u_ϕ^e denotes the electrical unknowns of the piezoelectric layer. The matrix M is the structural mass matrix and matrices $C_{\theta u}$ and $C_{\theta\phi}$ represent damping matrices due to thermal-mechanical coupling (piezocaloric) and thermal-electrical coupling (electrocaloric), respectively. The existence of these matrices in the governing equations leads to dissipation of thermal energy generated from mechanical and piezoelectric fields. The matrices C_{uu} and $C_{\theta\theta}$ are structural damping matrix and damping matrix representing thermal energy diffusion, respectively. The presence of all of these damping terms influences the dynamic response decay. The matrices $K_{u\phi}$ and $K_{\phi u}$ are stiffness matrices due to piezoelectric-mechanical coupling (converse piezoelectric and piezoelectric effects). Their presence allows piezoelectric materials to produce mechanical actuation forces under input voltages or electrical signals under mechanical deformations. The matrices $K_{u\theta}$ and $K_{\phi\theta}$ are stiffness matrices due to thermal-mechanical coupling (pyrostriction) and thermal-electrical coupling (pyroelectric), respectively. It must be noted that the thermal energy generated from mechanical and piezoelectric fields dissipates as damping ($C_{\theta u}$ and $C_{\theta\phi}$) while the mechanical and electrical energies generated from thermal field are retained as system stiffness. The matrices K_{uu} , $K_{\phi\phi}$ and $K_{\theta\theta}$ are stiffness matrices resulting from mechanical, electrical and thermal fields, respectively. The stiffness coupling effects can influence the equilibrium position if a steady state exists. The vectors F_u , F_ϕ and F_θ are force vectors due to mechanical, electrical and thermal fields, respectively. After static condensation, the equations of motion are reduced and

are expressed as

$$\begin{aligned} M\ddot{u}_u^e + C_{uu}\dot{u}_u^e + (K_{uu} - K_{u\phi}K_{\phi\phi}^{-1}K_{\phi u})u_u^e \\ + (K_{u\theta} - K_{u\phi}K_{\phi\phi}^{-1}K_{\phi\theta})u_\theta^e = F_u - K_{u\phi}K_{\phi\phi}^{-1}F_\phi \\ (C_{\theta u} - C_{\theta\phi}K_{\phi\phi}^{-1}K_{\phi u})\dot{u}_u^e + (C_{\theta\theta} - C_{\theta\phi}K_{\phi\phi}^{-1}K_{\phi\theta})\dot{u}_\theta^e + K_{\theta\theta}u_\theta^e = F_\theta \end{aligned} \quad (11)$$

Equation (11) can be written in state space form as follows.

$$\begin{aligned} \frac{d}{dt} \begin{Bmatrix} u_u^e \\ \dot{u}_u^e \\ u_\theta^e \end{Bmatrix} = \begin{bmatrix} 0 & I & 0 \\ -M^{-1}\hat{K}_{uu} & -M^{-1}C_{uu} & -M^{-1}\hat{K}_{u\theta} \\ 0 & -\hat{C}_{\theta\theta}^{-1}\hat{C}_{\theta u} & -\hat{C}_{\theta\theta}^{-1}K_{\theta\theta} \end{bmatrix} \begin{Bmatrix} u_u^e \\ \dot{u}_u^e \\ u_\theta^e \end{Bmatrix} \\ + \begin{Bmatrix} 0 \\ M^{-1}\hat{F}_u \\ \hat{C}_{\theta\theta}^{-1}F_\theta \end{Bmatrix} \{u\} \\ = Ax + Bu \end{aligned} \quad (12)$$

where the matrices A and B represent the system and input matrices, respectively.

LQG CONTROLLER DESIGN

Typically, it is impractical to measure all of the states in a system, as required in the Linear Quadratic Regulator (LQR) control scheme. Even if this were possible, the measurement would be contaminated by noise. Therefore, the LQG scheme is adopted to design a control system for vibration suppression of the composite shell with distributed self-sensing piezoelectric actuators. Using LQG theory with disturbance and sensor noise, the equations of motion (Equation (12)) can be written in state space form as follows (Nam et al., 2000).

$$\begin{aligned} \dot{x}(t) &= Ax(t) + Bu(t) + w(t) \\ y(t) &= Cx(t) + v(t) \end{aligned} \quad (13)$$

where $x(t)$, $u(t)$ and $y(t)$ represent the state, input and output vectors, respectively and matrices A , B and C are the system, input and measurement matrices, respectively. The disturbance $w(t)$ and sensor noise $v(t)$ are both assumed to be stationary, zero mean, Gaussian white, and to have covariance matrices satisfying

$$\begin{aligned} E\{w(t)w^T(1)\} &= W\delta(1-t) \\ E\{v(t)v^T(1)\} &= V\delta(1-t) \\ E\{w(t)v^T(1)\} &= 0 \end{aligned} \quad (14)$$

where $E[\bullet]$ denotes the expected value, δ denotes the Kronecker delta, and W and V represent the intensities of the disturbance and the sensor noise and are assumed to be positive definite.

A set of LQG controllers is designed as follows.

$$\begin{aligned} \dot{\hat{x}}(t) &= A\hat{x}(t) + Bu(t) + L[y(t) - C\hat{x}(t)] \\ u(t) &= K\hat{x}(t) \end{aligned} \quad (15)$$

where \hat{x} denotes the estimated state and K , L are the gain matrix and the Kalman filter gain matrix, respectively. The control input can be determined subject to minimizing the performance index, which is expressed as follows.

$$J = E \sum_{t=1}^{\infty} [X^T(t)Qx(t) + u^T(t)Ru(t)] \quad (16)$$

where matrices Q and R are positive semi-definite and positive definite, respectively. The optimal feedback

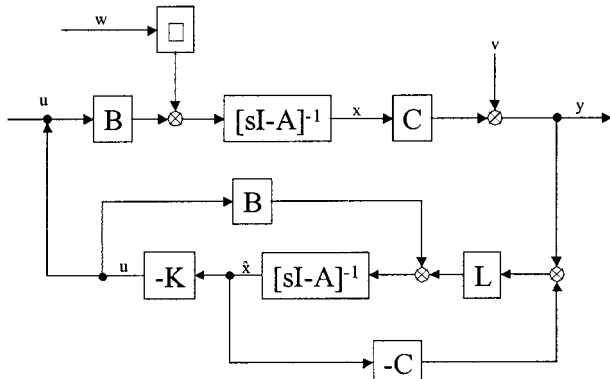


Figure 2. Block diagram of linear quadratic gaussian control scheme.

gain matrix K and the Kalman filter gain matrix L are obtained from

$$\begin{aligned} K &= (R + B^T PB)B^T PA \\ L &= A \sum C^T (C \sum C^T + V)^{-1} \end{aligned} \quad (17)$$

where P and Σ are the positive definite solutions of the following Riccati equations

$$\begin{aligned} A^T PA - P - A^T PB(R + B^T PB)^{-1} B^T PA + Q &= 0 \\ A \sum A^T - \sum -A \sum C^T (C \sum C^T + V)^{-1} C \sum A^T \\ + W &= 0 \end{aligned} \quad (18)$$

A block diagram of the LQG control problem is shown in Figure 2.

RESULTS AND DISCUSSIONS

Figure 1 shows the structural model used in the numerical analysis, which is a cylindrical fiber-reinforced laminated composite shell with nine surface bonded piezoelectric self-sensing actuators. The cylinder is simply-supported along boundaries and can be considered a part of a stiffened shell structure. The dimensions of the cylinder are such that length $L=0.6$ m, radius $R=0.3$ m and span angle $\phi=\pi/3$. Two different thickness ratios are considered in this work, $R/h=100$ and $R/h=200$. The fiber orientation is measured with respect to the length of the cylinder (β axis). The arc length of the cylinder, $\alpha=R\phi$. Each piezoelectric actuator has a length, $a_p=\alpha/7$, width, $b_p=L/7$, and thickness, $h_p=0.25$ h. The material constants for the composite and the piezoelectric material are listed in Table 1. In the numerical results presented,

Table 1. Material properties of piezoelectric and graphite-epoxy composite.

PZT	Graphite-Epoxy		PZT	Graphite-Epoxy
Elastic moduli (GPa):			Piezoelectric charge constant (pm/V):	
E_{11}	63	144.23	$e_{31} = e_{32}$	150
E_{22}	63	9.65	Electric permittivity (nf/m):	
E_{33}	63	9.65	b_{33}	15.0
Shear moduli (GPa):			b_{33}	15.0
G_{23}	24.6	3.45	Pyroelectric constant ($\mu C/m^2 \cdot ^\circ C$)	
G_{13}	24.6	4.14	d_3	20
G_{12}	24.6	4.14	Thermal conductivity ($W/m \cdot ^\circ C$):	
Poisson's ratio:			κ_{11}	2.1
ν	0.28	0.3	κ_{33}	2.1
Coefficients of thermal expansion ($\mu m / ^\circ C$):			Heat capacity ($J/Kg \cdot ^\circ C$)	
α_{11}	0.9	1.1	c_E	420
α_{33}	0.9	25.2	Thermal convection coefficient ($W/m^2 \cdot ^\circ C$)	
Density (kg/m^3)			h_v	20.0
ρ	7600	1389.23		

all deflections are nondimensionalized using the thickness of the primary structure.

To verify the accuracy of the improved layerwise theory in modeling dynamic response of the composite shell with distributed piezoelectric actuators, comparison of the fundamental natural frequency with NASTRAN solution is performed. CQUAD4 element of NASTRAN and three different ply layups, $[\theta_3/0_3]$, $[\theta_2/0_2/\theta_2]$ and $[\theta_2/0_2/-\theta_2]$ are used in this numerical study. Table 2 presents the nondimensionalized fundamental frequencies of the balanced ($[\theta_2/0_2/-\theta_2]$) and the unbalanced ($[\theta_2/0_2/\theta_2]$) cylindrical shells ($R/h=100$). The relative difference between NASTRAN and present results is 2.3% for the balanced laminate and 2.7% for the unbalanced laminate with $\theta=30$. In general, NASTRAN underpredicts the frequencies compared to the present theory. This is due to the fact that the present theory can provide accurate description of transverse shear stresses.

In most reported works, only the standard (“uncoupled”) model, with one-way coupling between mechanical, electrical and thermal fields, is considered.

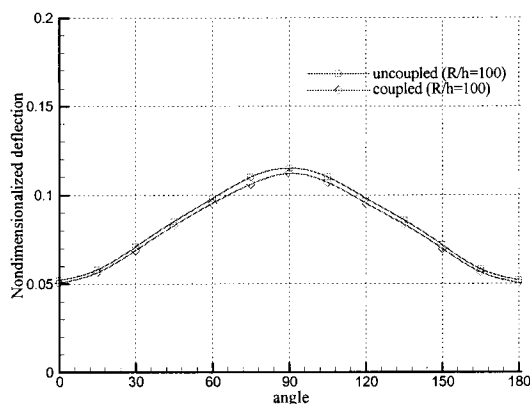
Table 2. Nondimensionalized fundamental frequencies of laminated cylindrical shells with piezoelectric actuators ($\bar{\omega} = \omega(L^2/h)\sqrt{\rho/E_2}$).

Laminated Angle(θ)	Balance Laminates ($\theta_2/0_2/\theta_2$)		Unbalance Laminates ($\theta_2/0_2/\theta_2$)	
	NASTRAN	Present	NASTRAN	Present
	0	8.9624	9.1697	8.9624
15	8.5880	8.8089	8.8501	9.0274
30	7.8141	8.0000	8.6254	8.8676
45	7.1150	6.8541	8.2634	8.3246
60	6.4410	6.1514	7.1400	7.3135
75	5.9916	5.8268	5.5672	5.8793
90	5.3675	5.6184	5.3675	5.6184

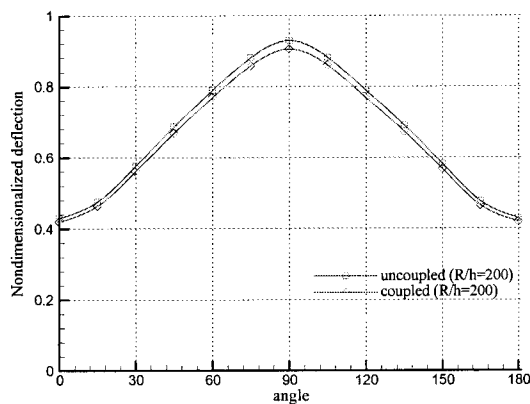
It must be noted that the uncoupled model neglects coupling effects on both equilibrium position (steady state) and energy dissipation due to damping. For example, in the analysis of piezoelectric actuators under electrical loads, using the uncoupled model, only converse piezoelectric effects can be considered. Piezoelectric effects are neglected. To illustrate the importance of two-way coupling effects, comparisons between the completely coupled t-p-m model and the uncoupled model are presented. It is expected that the bending-torsion coupling of the primary composite structure as well as the actuator locations influence the effects of distributed piezoelectric actuation. Thus, parametric studies are conducted and numerical results are presented to illustrate these effects.

Piezoelectric actuators are surface bonded on the top and bottom surface of the composite cylinder. The top and the bottom actuators are subjected to a step voltage load of the same magnitude but opposite directions, making out-of-plane deformation dominant. In this case, the t-p-m model represents two-way mechanical-piezoelectric coupling (piezoelectric and converse piezoelectric effect). The steady state center deflection of the $[\theta_3/0_3]$ laminated cylinder, due to piezoelectric actuation of 200 V, with two different thickness ratios ($R/h=100$ and 200) are presented in Figure 3. As seen from this figure, the coupled model predicts a smaller deflection compared to the uncoupled model. This is because accurate estimation of transformation of mechanical energy into thermal and electric energies, due to two-way coupling effects, is included in the t-p-m model. The relative differences between coupled and uncoupled model are 2.7% for $[0_3/0_3]$ laminate and 2.4% for $[90_3/0_3]$ laminate for $R/h=200$. The fact that the uncoupled model overpredicts the equilibrium position also implies that it overestimates the piezoelectric actuation effects.

To illustrate the effects of bending-torsion coupling of the primary structure, on actuation, parametric studies



(a) $R/h=100$



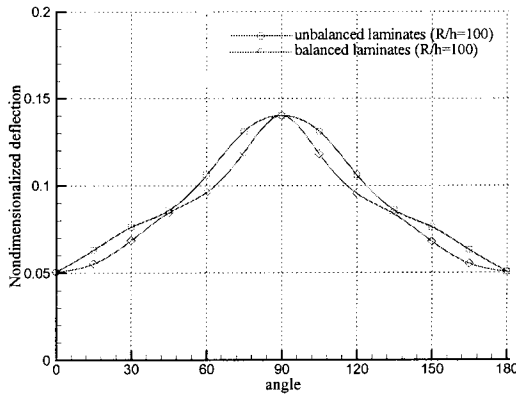
(b) $R/h=200$

Figure 3. Steady state center deflection of the cylindrical laminate under 200 V ($[\theta_3/0_3]$).

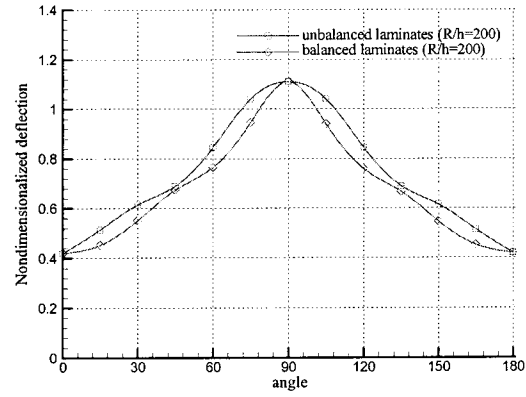
are conducted using two different lamination schemes, balanced ($[\theta_2/0_2/-\theta_2]$) and unbalanced ($[\theta_2/0_2/\theta_2]$). The steady state center deflections of the balanced and the unbalanced cylindrical laminates due to piezoelectric actuation of 200 V, for the two thickness ratios ($R/h = 100$ and $R/h = 200$) are presented in Figure 4. For the same voltage, the center deflection increases with increase in the lamination angle from zero to 90° . This is because an increase in lamination angle decreases the

bending stiffness of the primary structure. Similar trends are observed between 90 and 180° due to geometric symmetry. The unbalanced laminate predicts larger deflection compared to the balanced laminate for both thickness ratios. This is due to bending-torsion coupling in unbalanced laminates, which results in increased induced strain effects.

The bending-torsion couplings are illustrated using mode shapes. Figures 5 and 6 show the first and the



(a) $R/h=100$



(b) $R/h=200$

Figure 4. Steady state center deflection of the cylindrical laminate under 200 V ($[\theta_2/0_2/-\theta_2]$), ($[\theta_2/0_2/\theta_2]$).

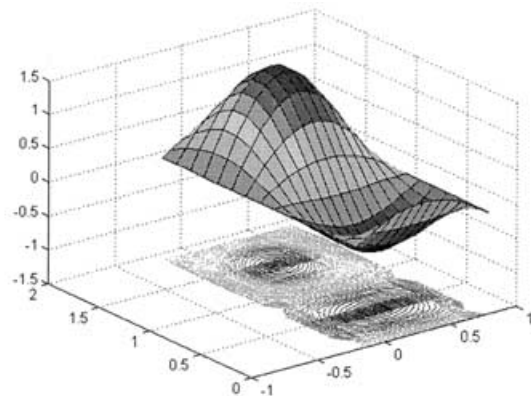
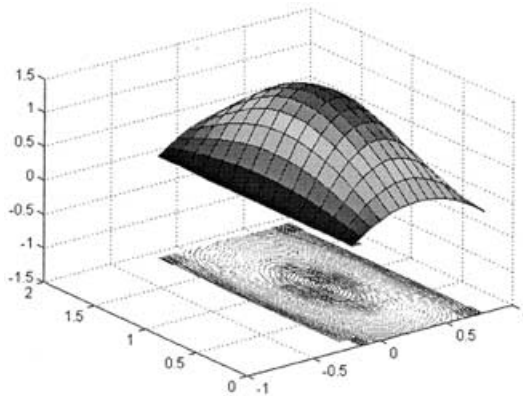


Figure 5. First and second mode shape of balanced cylindrical laminate ($[45_2/0_2/-45_2]$, $R/h = 100$).

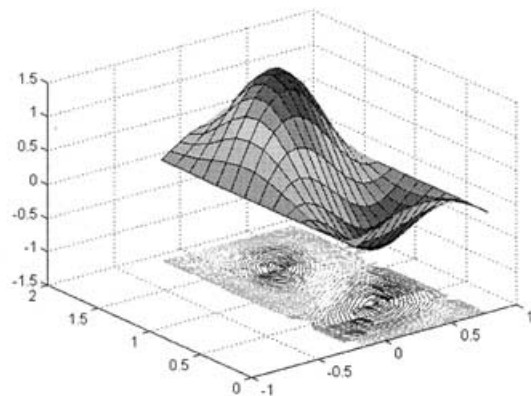
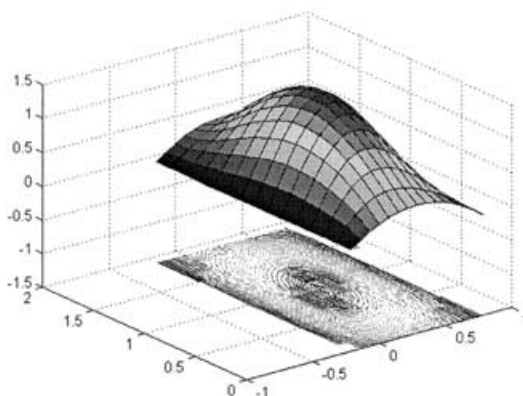


Figure 6. First and second mode shape of unbalanced cylindrical laminate ($[45_2/0_2/45_2]$, $R/h = 100$).

second mode shapes of the balanced ($[45_2/0_2/-45_2]$) and the unbalanced ($[45_2/0_2/45_2]$) cylindrical laminate with $R/h = 100$. As seen from these figures, the balanced laminate does not exhibit coupling between bending and torsion modes, while the unbalanced laminates show bending-torsion coupling, which is particularly significant in the second mode. Since actuators AC2, AC5 and AC8 are placed along the center line (Figure 1), the

piezoelectric actuation effects due to these actuators are not significant for the balanced laminate, particularly in the case of second mode excitation. This phenomenon is verified next using only second mode excitation.

Figures 7 and 8 show voltage histories of each actuator for the balanced ($[45_2/0_2/-45_2]$) and the unbalanced ($[45_2/0_2/45_2]$) laminate, respectively, under second mode excitation. It is observed that the actuators

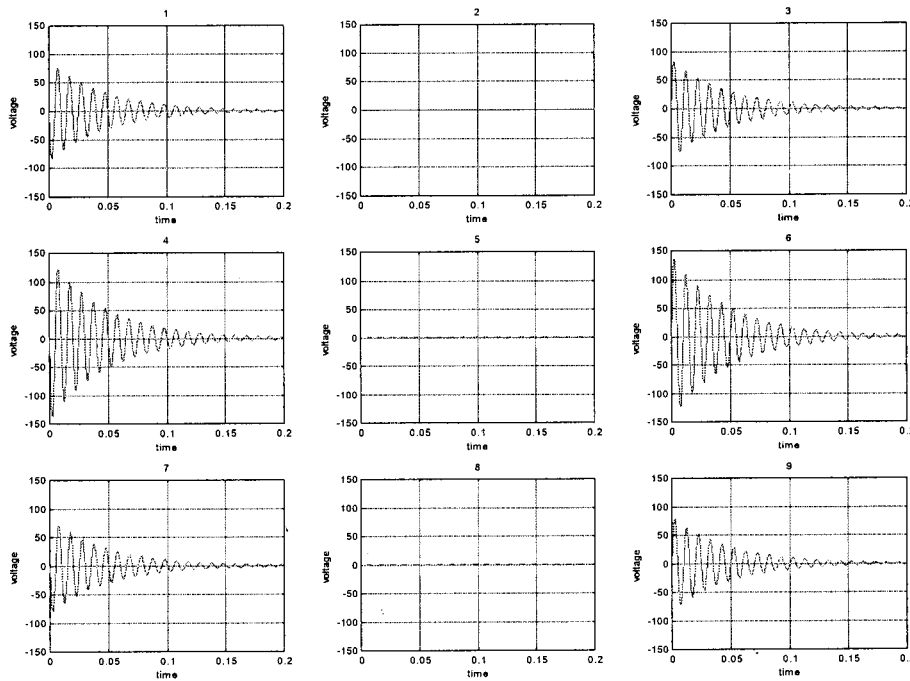


Figure 7. Voltage history of each actuator for balanced cylindrical laminate ($R/h = 100$ and $[45_2/0_2/-45_2]$).

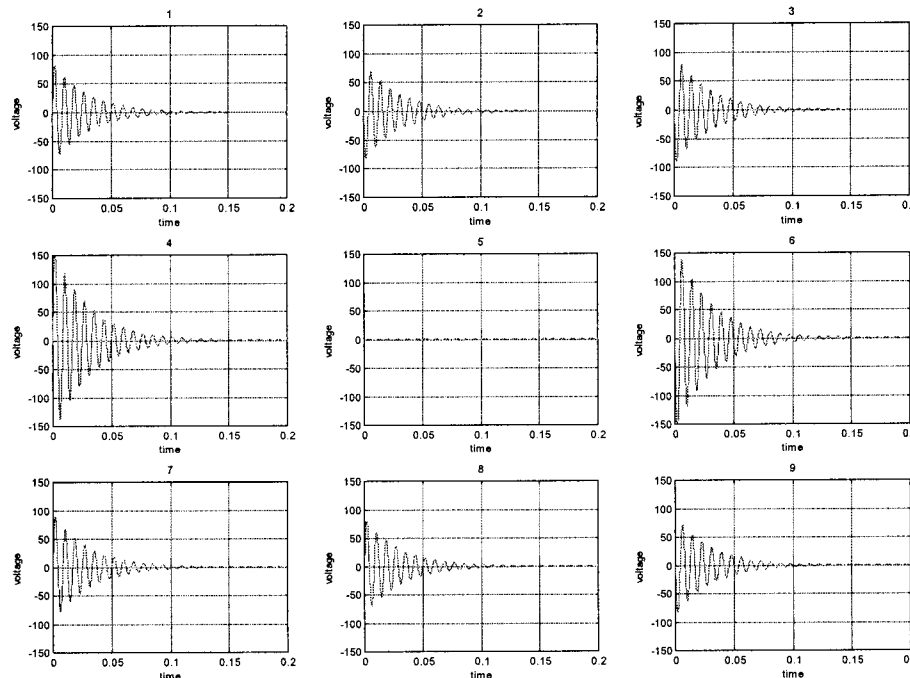


Figure 8. Voltage history of each actuator for unbalanced cylindrical laminate ($R/h = 100$ and $[45_2/0_2/45_2]$).

located along the center line (AC2, AC5 and AC8) of the balanced cylindrical laminate show zero actuation effects due to the symmetric excitation. However, in case of the unbalanced laminate, the actuators located close to the boundaries along the center line (AC2 and AC8) show piezoelectric actuation effects. This is once again caused by the bending-torsion coupling of the primary structure, as shown in Figures 5 and 6. It is also observed that the actuators located on the opposite side (AC1-AC3, AC4-AC6 and AC7-AC9) show 180° phase difference in both cases. In case of the unbalanced laminate, the actuators located along the center line (AC2 and AC8) exhibit the 180° phase difference in an effort to suppress the second mode. The center actuator AC5 shows no actuation effect in the second mode excitation for both the balanced and the unbalanced laminates. However, this actuator plays an important role in first and third mode excitations.

Since the damping ratios of these modes are of interest in this study, in LQG control, the matrix Q is defined such that more weight is placed on these three modes. That is, Q is taken to be identity matrix except for the terms corresponding to the aforementioned modes. The variation of the first three closed loop damping ratios with laminate angle, for the shell with $R/h = 100$ and stacking sequence $([\theta_3/0_3])$, are presented in Figure 9. All three closed loop damping ratios increase with increase in the laminate angle from zero to 90°. This is due to two reasons. First, structural natural frequencies decrease with increase in the laminate angle and second, piezoelectric actuation effects are affected by the bending-torsion coupling of the primary structure. The uncoupled model over-predicts closed loop damping ratios. This can be explained as follows. The steady state deflections presented in Figure 3 shows that the deflection predicted by the uncoupled model, due to external piezoelectric actuation, is larger compared to that obtained using the t-p-m model under the same actuation. This implies that if piezoelectric force is used to control deflection, the uncoupled theory will overestimate control authority.

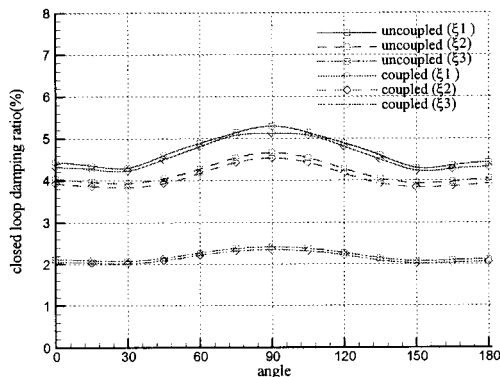


Figure 9. Variation in closed loop damping ratio with stacking sequence; coupled and uncoupled model $([\theta_3/0_3], R/h = 100)$.

This is true over the entire range of stacking sequence. The relative differences in the closed loop damping ratios for the first mode, between the uncoupled and the coupled model, is 2.74% for the $[0_3/0_3]$ laminate and 3.30% for the $[90_3/0_3]$ laminate.

Figure 10 presents variations of the first three closed loop damping ratios with laminate angle for balanced and unbalanced laminated shell with $R/h = 60$. The closed loop damping ratios of the unbalanced laminate are larger compared to those of the balanced laminate due to bending-torsion coupling. The maximum difference in the closed loop damping ratio is observed in the case with maximum bending-torsion coupling, that is $\theta = 45^\circ$. The maximum relative difference in damping ratio associated with the first mode, between the balanced and the unbalanced laminate, is 38%. As expected, the distribution of the closed loop damping ratios is symmetric over variations in ply angles between zero and 90° and 90 and 180°. Similar trends are observed for the second and third mode damping ratios. Figures 11 and 12 show similar comparisons for shell with $R/h = 100$ and $R/h = 200$, respectively. The same weighting matrix Q , as in the case with $R/h = 60$, is used.

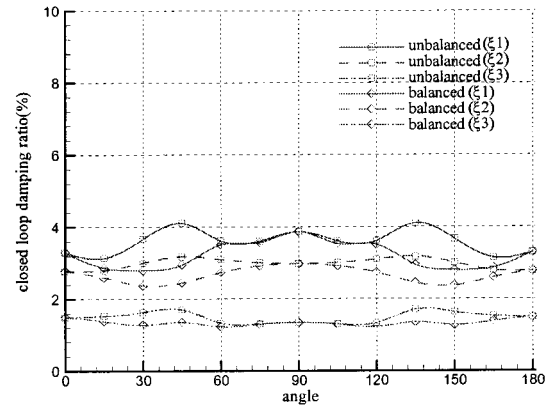


Figure 10. Variation in close loop damping ratio with stacking sequence; balanced and unbalanced cylindrical laminate $(R/h = 60)$.

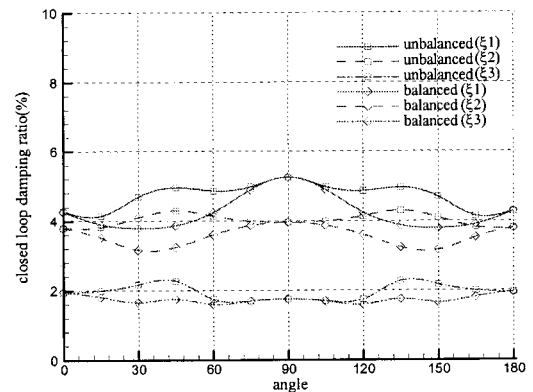


Figure 11. Variation in close loop damping ratio with stacking sequence; balanced and unbalanced cylindrical laminate $(R/h = 100)$.

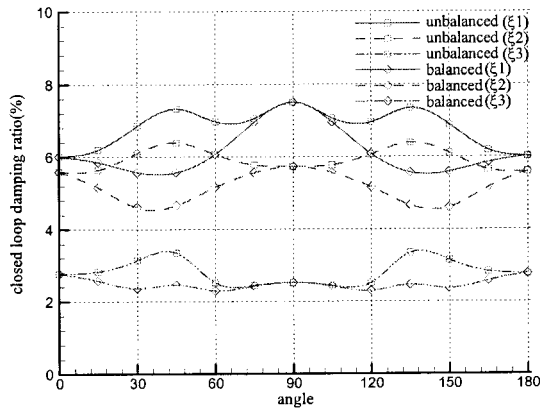


Figure 12. Variation in close loop damping ratio with stacking sequence; balanced and unbalanced cylindrical laminate ($R/h=200$).

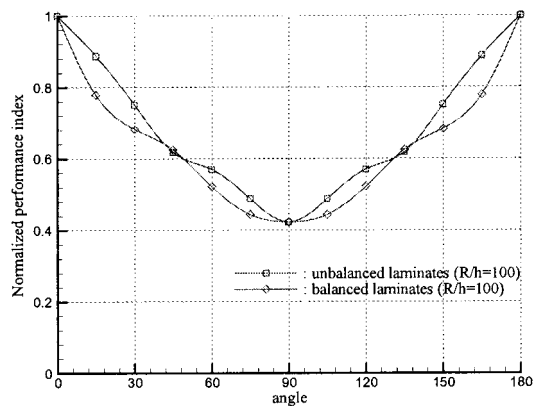


Figure 13. Variation in performance index with stacking sequence; balanced and unbalanced cylindrical laminate ($R/h=100$).

As seen from Figures 11 and 12, the values of the closed loop damping ratios are larger, compared to the case with $R/h=60$, in both balanced and unbalanced cases due to decrease in system stiffness. Once again, the piezoelectric actuation effects are more pronounced in the unbalanced laminate compared to the balanced laminate. The maximum relative difference in the first mode closed loop damping ratio, between balanced and unbalanced laminates, for both R/h values is exhibited at $\theta=45^\circ$ where maximum bending-torsion occurs. These values are 28% for $R/h=100$ and 32% for $R/h=200$. The variation in the minimum value of performance index with stacking sequence is presented in Figure 13. The minimum value of performance index reduces with the decrease in the system stiffness. The value of performance index at $\theta=90^\circ$ is 43% compared to that at $\theta=0^\circ$. The performance index variation shows opposite pattern of steady state center deflection shown in Figure 4. It is observed that the structural flexibility leads to higher damping ratio as well as lower value of performance index.

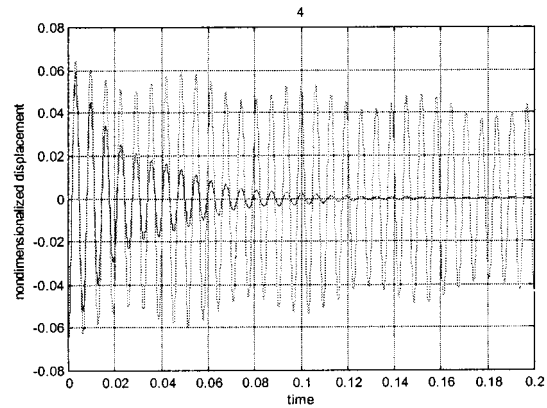


Figure 14. Open loop and closed loop time responses at the center of the cylinder ($R/h=60$, $[0_2/0_2/0_2]$).

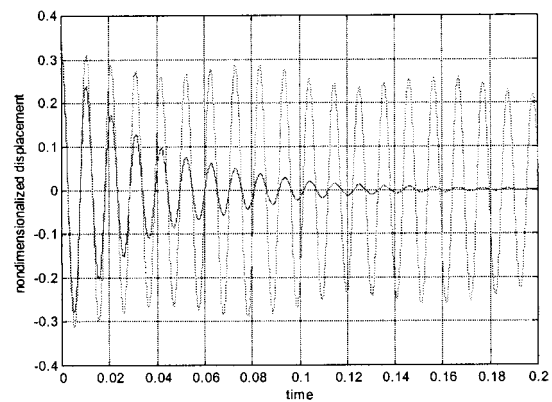


Figure 15. Open loop and closed loop time responses at the center of the cylinder ($R/h=100$, $[0_2/0_2/0_2]$).

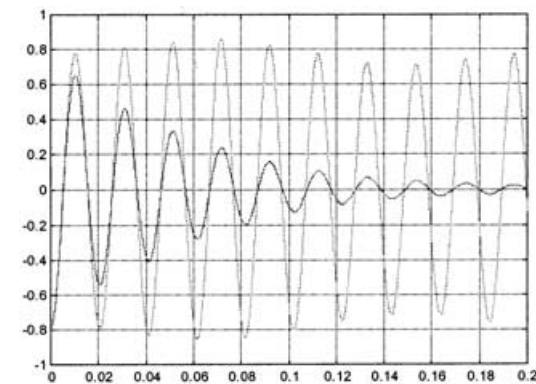


Figure 16. Open loop and closed loop time responses at the center of the cylinder ($R/h=200$, $[0_2/0_2/0_2]$).

Next, the time responses of the open loop and the closed loop systems, excited using a combination of 80% of the first mode, 18% of the second mode and 2% of the third mode, are presented for balanced cylindrical laminates with $[0_2/0_2/0_2]$ stacking sequence and thickness ratios $R/h=60$ (Figure 14), $R/h=100$ (Figure 15) and $R/h=200$ (Figure 16). As seen from these figures, the amplitude of deflection is reduced dramatically with

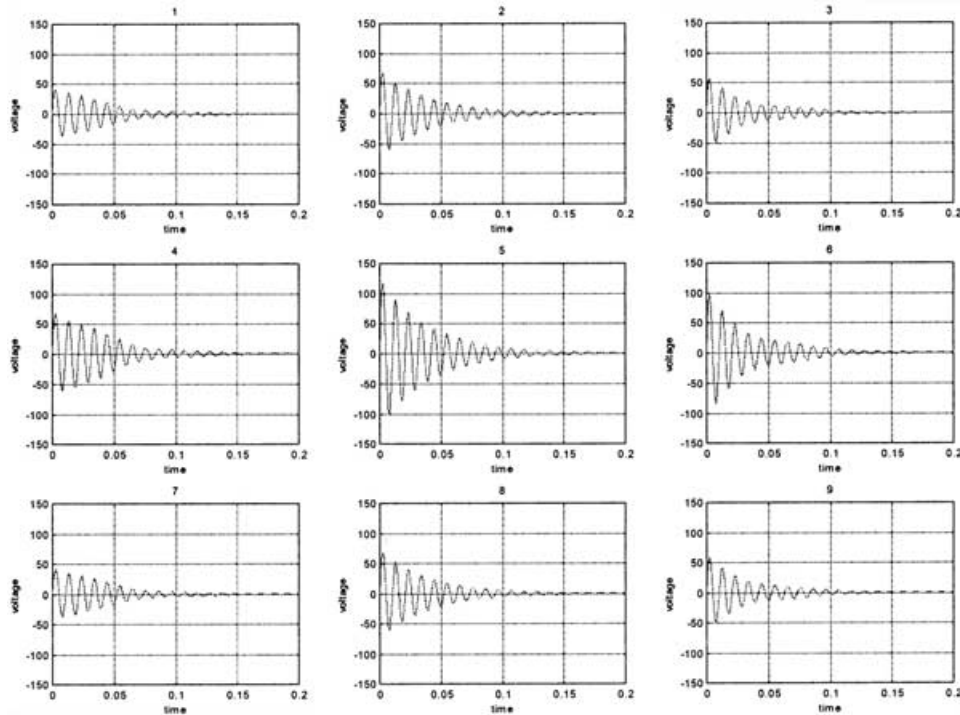


Figure 17. Voltage history of each actuator ($R/h=100$, $([0_2/0_2/0_2])$).

the application of control in both cases. The corresponding control voltage histories of each actuator are presented in Figure 17 for the case with $R/h=100$. The actuator located at the center shows maximum actuation effect in order to suppress the first mode which is dominant.

CONCLUDING REMARKS

A completely coupled t-p-m theory, based on the improved layerwise displacement field and higher order electrical and temperature fields, was developed to study dynamic responses and control effects of smart composite shells. The theory was implemented using a finite element technique that ensures the application to practical geometry and boundary conditions. Numerical analysis was conducted for simply-supported cylindrical shells with distributed self-sensing piezoelectric actuators. Comparisons were made with three dimensional NASTRAN solutions to verify the accuracy of the developed theory. Control authority was investigated using LQG theory. Parametric studies were conducted to investigate the effects of the two-way coupling, actuator location and bending-torsion coupling and flexibility of the host structure. The following important observations were made from this study:

1. The developed approach provides a means to accurately model the dynamic behavior of laminated

composite shells with distributed piezoelectric actuators.

2. Comparison of natural frequencies shows very good correlations with NASTRAN solution.
3. The uncoupled model, which neglects the two-way coupling effects, overestimates steady state equilibrium position and control authority in closed loop control.
4. The piezoelectric actuation effects are significantly affected by bending and torsion coupling and flexibility of the primary structures as well as placement of the actuators.
5. Closed loop damping ratios increase with decrease in structural stiffness, that is, increase in R/h ratio.

ACKNOWLEDGMENT

The research is supported by NASA Langley Research Center, grant number NAG-1-2283, technical monitor Dr. D. Ambur.

REFERENCES

- Anderson, E. H. and Hagood, N. W. 1994. "Simultaneous Piezoelectric Sensing/Actuation: Analysis and Application to Controlled Structures," *Journal of Sound and Vibration*, 174:617-639.
- Chattopadhyay, A., Li, J. and Gu, H. 1998a. "A Coupled Thermo-Piezoelectric-Mechanical Model For Smart Composite Laminates,"

- In: *Proceedings of the AIAA/ASME/ASCE/AHS/ASC 39th Structures, Structural Dynamics and Materials Conference*, pp. 2902–2910.
- Chattopadhyay, A., Gu, H. and Li, J. 1998b. “A Coupled Thermo-Piezoelectric-Mechanical Theory For Smart Composites Under Thermal Load,” In: *Proceedings of Ninth International Conference On Adaptive Structures & Technologies*, Cambridge, MA.
- Crawley, E. F. and Luis, J. 1987. “Use of Piezoelectric Actuators as Elements of Intelligent Structures,” *AIAA Journal*, 25:1373–1385.
- Kim, H. S., Zhou, X. and Chattopadhyay, A. (2001). “Interlaminar Stress Analysis of Shell Structures with Piezoelectric Patch Including Thermal Loading,” *SPIE's 8th International Symposium on Smart Structures and Materials*, Newport Beach, CA, 4326:364–375.
- Lee, C. K. 1990. “Theory of Laminated Piezoelectric Plates for the Design of Distributed Sensors/Actuators. Part 1: Governing Equations and Reciprocal Relationships,” *Journal of the Acoustical Society of America*, 87:1144–1158.
- Lee, H. and Saravanos, D. A. 1996. “The Effect of Temperature Induced Material Property Variations on Piezoelectric Composite Plates,” In: *Proceedings of the AIAA/ASME/ASCE/AHS/ASC 37th Structures, Structural Dynamics and Materials Conference*, pp. 1781–1788.
- Lee, H. and Saravanos, D. A. 1997. “Active Compensation of Thermally Induced Bending and Twisting in Piezoceramic Composite Plates,” In: *Proceedings of the AIAA/ASME/ASCE/AHS/ASC 38th Structures, Structural Dynamics and Materials Conference*, pp. 120–130.
- Mindlin, R. D. 1974. “Equations of High Frequency Vibrations of Thermopiezoelectric Crystal Plates,” *International Journal of Solids Structure*, 10: 625–632.
- Mitchell, J. A. and Reddy, J. N. 1995a. “A Refined Hybrid Plate Theory for Composite Laminates with Piezoelectric Laminae,” *International Journal of Solids Structure*, 32:2345–2367.
- Mitchell, J. A. and Reddy, J. N. 1995b. “A Study of Embedded Piezoelectric Layers in Composite Cylinders,” *Journal of Applied Mechanics*, 62:166–173.
- Mukherjee, N. and Sinha, P. K. 1993. “A Finite Element Analysis of Thermostructural Behavior of Composite Plates,” *Journal of Reinforced Plastics and Composites*, 12:1026–1042.
- Nam, C., Chen, P. C., Liu, D., Kim, J. and Chattopadhyay, A. 2000. “Neural Net-based Controller for Flutter Suppression Using ASTROS* with Smart Structures,” In: *Proceedings SPIE's 7th International Symposium on Smart Structures and Materials*, 3985:98–109.
- Tauchert, T. R. 1992. “Piezothermoelastic Behavior of a Laminated Plate,” *Journal of Thermal Stresses*, 15:25–37.
- Thornburgh, R. P. and Chattopadhyay, A. 2001. “Electrical-Mechanical Coupling Effects on the Dynamic Response of Smart Composite Structures,” In: *Proceedings of the International Society for Optical Engineering*, 4327:413–424.
- Tzou, H. S. and Bao, Y. 1995. “A Theory on Anisotropic Piezothermoelastic Shell Laminates with Sensor/Actuator Applications,” *Journal of Sound and Vibration*, 184:453–473.
- Zhou, X., Chattopadhyay, A. and Gu, H. 2000. “Dynamic Response of Smart Composites Using a Coupled Thermo-Piezoelectric-Mechanical Model,” *AIAA Journal*, 38:1939–1948.
- Zhou, X. and Chattopadhyay, A. 2001. “An Improved Shear Deformation Theory for Laminated Shells Addressing Transverse Stress Continuity,” In: *Proceedings of the AIAA/ASME/ASCE/AHS/ASC 42th Structures, Structural Dynamics and Materials Conference*, pp. 2001–1338.